Nano-Micro Letters

e-ISSN 2150-5551
CN 31-2103/TB

ARTICLE

https://doi.org/10.1007/s40820-025-01977-w

Cite as
Nano-Micro Lett.
(2026) 18:131

Received: 10 July 2025
Accepted: 11 October 2025

High-Performance Cu-Based Liquid Thermocells Enabled by Thermosensitive Crystallization and Etched Carbon Cloth Electrode

Wei Fang[1], Zeping Ou[1], Yifan Wang[1], Zhe Li[1], Qian Huang[1], Pengchi Zhang[1], Xinzhe Li[1], Yujie Zheng[1], Lijun Hu[2], Chen Li[1,3], Jianyong Ouyang[4], Kuan Sun[1] ✉

HIGHLIGHTS

- A novel Cu^{+}/Cu^{2+} redox couple was introduced to enable a thermosensitive crystallization process, significantly enhancing thermopower from 1.47 to 2.93 mV K^{-1}.
- A readily fabricated etched carbon cloth electrode offered an enlarged electroactive surface area, demonstrating superior current density through improved kinetics.
- The optimized Cu^{+}/Cu^{2+} system, achieved through synergistic enhancements in thermodynamic and kinetic performance, delivered an outstanding normalized power density $P_{max}\,(\Delta T)^{-2}$ of 3.97 mW m^{-2} K^{-2}.

ABSTRACT Thermocells are garnering increasing attention as a promising thermoelectric technology for harvesting low-grade heat. However, their performance is often limited by the scarcity of high-performance redox couples that possess both high thermopower and rapid redox kinetics. This work addresses this challenge by leveraging our recently developed copper (I/II) (Cu^{+}/Cu^{2+}) redox couple. We significantly enhance the performance of Cu-based liquid thermocells by integrating a thermosensitive crystallization process with etched carbon cloth electrodes, achieving synergistic improvements in thermodynamic and kinetic performance. The thermosensitive crystallization process establishes a persistent Cu^{2+} concentration gradient, boosting the thermopower from 1.47 to 2.93 mV K^{-1}. Moreover, the etched carbon cloth electrodes provide a larger electroactive surface area and demonstrate a higher current density. Consequently, the optimized Cu^{+}/Cu^{2+} system achieved an exceptional normalized power density $P_{max}\,(\Delta T)^{-2}$ of 3.97 mW m^{-2} K^{-2}. A thermocell module comprised of 20 cells directly power various electronic devices at a temperature difference of 40 K. This work successfully exhibits potential of Cu^{+}/Cu^{2+} redox couple in thermoelectric conversion and introduces a valuable redox couple for high-performance thermocells.

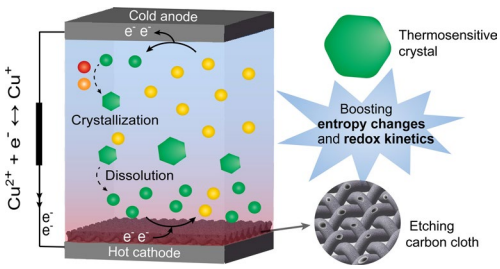

KEYWORDS Thermocell; Thermosensitive crystallization; Porous carbon electrode; Power density; Low-grade heat harvest

✉ Kuan Sun, kuan.sun@cqu.edu.cn
[1] MOE Key Laboratory of Low-Grade Energy Utilization Technologies and Systems, School of Energy and Power Engineering, Chongqing University, Chongqing 400044, People's Republic of China
[2] Hunan Key Laboratory for the Design and Application of Actinide Complexes, School of Chemistry and Chemical Engineering, University of South China, Hengyang 421001, Hunan, People's Republic of China
[3] Sibley School of Mechanical and Aerospace Engineering, Cornell University, Ithaca, NY 14853, USA
[4] Department of Materials Science and Engineering, National University of Singapore, Singapore 117574, Singapore

Published online: 05 January 2026

1 Introduction

As global energy demands continue to rise and the search for sustainable energy solutions intensifies, the efficient utilization of available thermal energy resources, especially those that are often neglected, becomes increasingly critical [1, 2]. Low-grade heat, defined as thermal energy below 100 °C, is an often-overlooked and underutilized resource. It is abundantly available in various environmental sources, including geothermal and solar-thermal energy, as well as waste heat generated by power plants, data centers, and even the human body [3, 4]. Thermoelectric technologies, which convert this ubiquitous thermal energy directly into useful electricity, hold significant potential for powering low-energy smart devices within the Internet of Things (IoT) [5–7]. Among them, liquid thermocells (LTCs) present a promising new solution, offering high thermopower (in the mV K^{-1} range), low cost, and easy scalability. LTCs exploit the temperature dependence of electrochemical redox potentials, known as the thermogalvanic effect, to generate continuous electricity. The power output ($P = V \bullet J$) of LTCs depends on both thermodynamic and kinetic features. The thermodynamic aspect is characterized by thermopower S_e, defined as $S_e = \partial V/\partial T = \Delta S/nF$, where ΔS represents the entropy change for the redox reaction, n is the number of electrons transferred, and F refers to Faraday's constant. The kinetic aspect is directly reflected in the current density (J). Overall, the normalized power density (P_{max} $(\Delta T)^{-2}$) serves as a comprehensive metric for evaluating and comparing the performance of TLCs.

Since the introduction of the concept of LTCs in the nineteenth century, only a limited number of redox couples have demonstrated potential for thermoelectric conversion, including $Fe(CN)_6^{3-}/Fe(CN)_6^{4-}$ [8–10], Fe^{2+}/Fe^{3+} [11, 12], Cu/Cu^{2+} [13, 14], I^-/I_3^- [15, 16], and others [17, 18]. Among these redox couple systems, the $Fe(CN)_6^{3-}/Fe(CN)_6^{4-}$ system stands out as the most preferred thermogalvanic system primarily due to its intrinsic characteristics. The pristine 0.4 M $Fe(CN)_6^{3-}/Fe(CN)_6^{4-}$ system exhibits a high S_e of approximately −1.4 mV K^{-1} and rapid redox kinetics, serving as a benchmark for LTC [19, 20]. Over the past decade, the field of LTCs has witnessed remarkable progress and impressive performance enhancements through advancements in electrolytes [10, 21–24], electrodes [25–27], and device architectures [28–30], particularly within the $Fe(CN)_6^{3-}/Fe(CN)_6^{4-}$ system. For instance, Duan et al. introduce strong chaotropic guanidinium cations and highly soluble urea into $Fe(CN)_6^{3-}/Fe(CN)_6^{4-}$ system, synergistically enlarging the entropy difference. This resulted in a high S_e of −4.2 mV K^{-1} and a normalized power density (P_{max} $(\Delta T)^{-2}$) of 1.1 mW K^{-2} m^{-2} [9]. Furthermore, carbon nanomaterials have emerged as cost-effective electrodes, providing high current densities in LTCs due to their increased surface area and rapid electron transfer kinetics [8, 31, 32]. For example, activated carbon cloth employed as electrodes in the $Fe(CN)_6^{3-}/Fe(CN)_6^{4-}$ system can achieve a P_{max} $(\Delta T)^{-2}$ of up to 1.80 mW K^{-2} m^{-2} [26]. In a holistic approach, Yu et al. pioneered a thermosensitive crystallization strategy in conjunction with porous carbon fiber electrodes, yielding a high S_e of −3.73 mV K^{-1} and a remarkable P_{max} $(\Delta T)^{-2}$ of 7.08 mW K^{-2} m^{-2} [28].

Conversely, other redox couple systems have struggled to exceed 2 mW K^{-2} m^{-2} due to intrinsic performance limitations. For example, applying similar thermosensitive crystallization and 3D multi-structured electrodes to enhance the thermodynamic and kinetic properties of the Cu/Cu^{2+} system yields a S_e of only 1.66 mV K^{-1} and a P_{max} $(\Delta T)^{-2}$ of 0.71 mW K^{-2} m^{-2} [13]. Although the I^-/I_3^- system achieves an exceptionally high S_e of 9.62 mV K^{-1} through strong hydrophobic interactions between thermoresponsive methylcellulose and I_3^- ions, it only reaches a P_{max} $(\Delta T)^{-2}$ of 0.36 mW K^{-2} m^{-2} [15]. This is attributed to the slow kinetic rate inherent to this system. Although optimized systems show significant improvements over their unoptimized counterparts, they still fall short when compared to the $Fe(CN)_6^{3-}/Fe(CN)_6^{4-}$ system. The Fe^{2+}/Fe^{3+} system displays a S_e that is highly dependent on the choice of counter ions, with the perchlorate system ($Fe(ClO_4)_2/Fe(ClO_4)_3$) yielding a relatively high S_e of ~1.65 mV K^{-1} [33, 34]. However, this system often requires expensive platinum electrodes to ensure fast kinetics and corrosion resistance. Utilizing highly catalytic electrodes in a cylindrical architecture, the $Fe(ClO_4)_2/Fe(ClO_4)_3$ system achieves a P_{max} $(\Delta T)^{-2}$ of 1.92 mW K^{-2} m^{-2} [35]. It is important to note that the advancement of high-performance LTCs is currently constrained by the challenge of discovering redox couples that exhibit both high S_e and rapid redox kinetics simultaneously.

Recently, we have developed an innovative redox couple, Cu^+/Cu^{2+} (Fig. 1, left), which demonstrate exceptional thermogalvanic performance. This system rivals

https://doi.org/10.1007/s40820-025-01977-w

the performance of the benchmark 0.4 M $K_3Fe(CN)_6$/$K_4Fe(CN)_6$ system, showcasing an intrinsically high S_e of 1.51 mV K^{-1} and fast redox kinetics. In this work, we achieve further performance enhancements by combining a thermosensitive crystallization process with etched carbon cloth electrodes, enabling synergistic optimization of both thermodynamic and kinetic properties. The thermosensitive crystallization process, driven by ammonium sulfate, creates a sustained Cu^{2+} concentration gradient that contributes to a substantial increase in entropy change (ΔS), thereby boosting the S_e from 1.47 to 2.93 mV K^{-1}. Additionally, the etched carbon cloth electrodes are prepared via an easily accessible alkalization and annealing treatment, which increases hydrophilicity and surface area. This results in a larger electroactive surface area and consequently leads to greater current density. As a result, the optimized Cu^+/Cu^{2+} system achieved an exceptionally high P_{max} $(\Delta T)^{-2}$ of 3.97 mW m^{-2} K^{-2}. Given to the high S_e and J of Cu^+/Cu^{2+} system, a prototype module consisting of 20 units generates an open-circuit voltage of 2.14 V and a maximum power output of 27.19 mW under a temperature difference (ΔT) of 40 K, which is sufficient to directly power low-energy power devices. This work successfully demonstrates the potential of the Cu^+/Cu^{2+} redox couple in thermoelectric conversion and introduces a valuable new redox couple for high-performance thermocells.

2 Experimental Section

2.1 Materials

Cuprous chloride (CuCl), cupric chloride ($CuCl_2$), potassium ferricyanide ($K_3Fe(CN)_6$), potassium ferrocyanide ($K_4Fe(CN)_6$), sodium sulfate (Na_2SO_4), potassium sulfate (K_2SO_4), ammonium sulfate ($(NH_4)_2SO_4$), tetramethylammonium sulfate, and guanidinium sulfate were obtained from Shanghai Aladdin Co. Ltd. Hydrochloric acid (HCl) and ammonium chloride (NH_4Cl) were purchased from the Chengdu Kelong Co. Ltd. All chemical reagents were used without further purification. Graphite sheets and carbon cloth were purchased from Longyao Carbon New Material Technology Co. Ltd. (China), respectively. The deionized water used in all experiments was prepared by an ATSro 10.

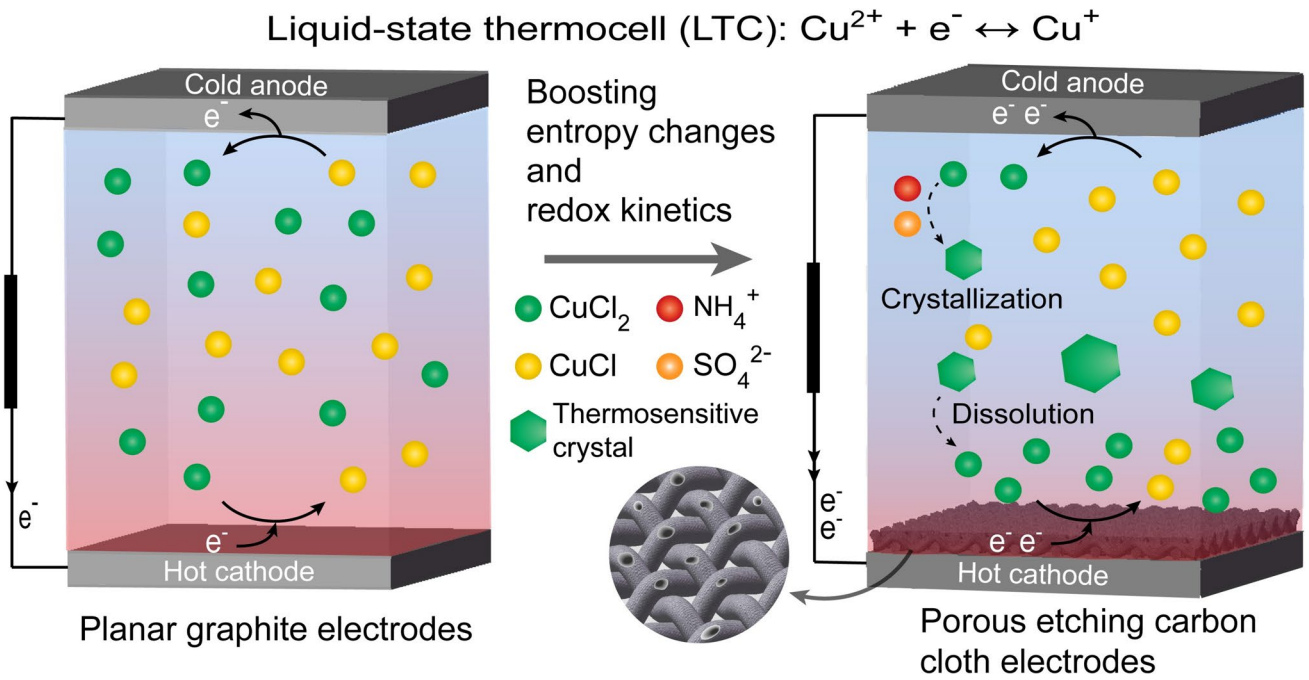

Fig. 1 Schematic representation of a high-performance Cu-based liquid thermocell. This design incorporates a thermosensitive crystallization process and etched carbon cloth electrodes to synergistically enhance entropy changes and redox reaction kinetics. The reduction reaction ($Cu^{2+} + e^- \rightarrow Cu^+$) occurs at the hot electrode (cathode), and the oxidation reaction ($Cu^+ \rightarrow Cu^{2+} + e.^-$) takes place at cold electrode (anode)

2.2 Preparation of Electrodes, Electrolytes and LTCs Devices

3D porous carbon cloth electrodes were prepared by two steps. First, carbon cloth was immersed in 1 M KOH solution at 70 °C for 24 h, stirred at 500 rpm. Thereafter, carbon cloth was washed with deionized water several times and dried in vacuum at 60 °C for 12 h. Second, carbon cloth was annealed at 600 °C in a tube furnace. The annealing time affected surface structure of carbon cloth fiber. We set five time points: 0, 1, 3, 5, and 7 h. The etched carbon cloth was washed and placed in the oven to dry for use.

For Cu-based liquid thermocell, CuCl and $CuCl_2$ were dissolved in this aqueous solution containing 0.1 M HCl and 0.9 M NH_4Cl. The 0.15 M CuCl and 0.4 M $CuCl_2$ dissolved in this aqueous solution were used as the pristine electrolyte for LTC. The optimized electrolyte was prepared by adding $(NH_4)_2SO_4$ into the pristine electrolyte. Similarly, the electrolyte with other molarity ratios and additives was prepared for comparison. Typically, a planar single cell was used to demonstrate the thermoelectric performance of the LTC/TC-LTC. As shown in Fig. S1, the planar cell was assembled by four steps: first, attaching the carbon cloth electrodes and/or graphite sheets to the poly (methyl methacrylate) (PMMA) frame and sealing with epoxy glue; second, injecting electrolyte to fill up the cell; third, sealing the cell by the nano transparent double-sided tape; forth, horizontally placing the cell to test. The cross-sectional area of the frame was 3.24 cm^2, and the height was 1.2 cm. The hot side was heated by an electrical heating plate, and the cold side was cooled by a thermoelectric cooler contacting a water-cooling plate. In all measurements, the cold electrode temperature is controlled at ~20 °C. A similar process was used to fabricate an integrated TC-LTC module (Fig. 5a). In brief, a plastic frame containing 20 isolated cells was filled with optimized electrolyte. Each isolated cell was the same size as the planar cell above. Finally, the isolated cells were connected in series by Cu wires.

2.3 Material and Electrical Characterizations

The concentration of Cu^{2+} and Cu^{+} in the electrolytes was measured by UV–Vis spectro-photometry (Shimadzu UV-3600) with the loading buffer diluted ~350 times by 3 M NH_4Cl solution. The crystal structure of samples was analyzed by X-ray diffraction (XRD, PANalytical X'Pert Powder). Fourier-transform infrared spectroscopy (FTIR) was performed using Thermo Fisher Scientific Nicolet iS50. X-ray photoelectron spectroscopy (XPS) was performed with an ESCALAB-250Xi X-ray photoelectron spectrometer. The solubility (defined as g per 100 g solution) of the crystals at different temperatures was directly measured. The dried samples were gradually added them to aqueous solution (contain 0.9 M NH_4Cl and 0.1 M HCl) (5 g) at different temperatures and thermostatically incubated until the solution was saturated. The amounts of dried samples added were multiplied by 20 to obtain their solubility at different temperatures. The morphology of the various electrodes was characterized by a scanning electron microscope (SEM, JXA-8530F Plus). The contact angles of water droplets on the various electrodes were measured by a contact angle meter (SL200B, Kino) at room temperature.

Cyclic voltammetry (CV) scanning was performed at 10 mV s^{-1}. The Randles–Sevcik equation is given by $I_p = 2.69 \times 10^5 \cdot \mathrm{ESA} \cdot D^{1/2} \cdot n^{3/2} \cdot \nu^{1/2} \cdot C$, where I_p is the faradaic peak current, n is the number of electrons transferred during the redox reaction, ESA is the electroactive surface area, C is the concentration of the probe molecule, ν is the potential scan rate, and D is the diffusion coefficient. Electrochemical impedance spectra (EIS) measurements were taken in the frequency range between 10 kHz and 100 mHz. CV and EIS tests were performed on electrochemical workstation (Bio-Logic, VMP3, SN 0897). Voltage–time, current–voltage, and power–voltage curves were measured with a Keithley 2400 instrument, and the corresponding temperature profiles were recorded by a thermocouple data logger (USB-TC-08, Pico Technology, St. Neots). The current–voltage curves were recorded by the points measured from the open-circuit voltage to 0 V, and the power–voltage curves were calculated by the product of the corresponding current and voltage values.

3 Results and Discussion

The LTC consists of an electrolyte containing a redox couple sandwiched between two electrodes (Fig. 1, left). The device architecture is straightforward and does not require complex manufacturing processes, demonstrating good reliability (Figs. S1 and S2). Our laboratory has developed a novel redox couple, Cu^{+}/Cu^{2+}, achieved by stabilizing

https://doi.org/10.1007/s40820-025-01977-w

cuprous ions in chloride-rich solutions. The solubility of $CuCl/CuCl_2$ in an electrolyte solution of 0.9 M NH_4Cl and 0.1 M HCl can reach up to 0.15 M, yielding an inherent S_e as high as 1.51 mV K^{-1} (Fig. S3). This promising pristine system presents significant opportunities for further improvement. As detailed in Note S1, the potential difference under a temperature difference (also referred to as S_e) depends on both the solvent-dependent entropy difference (ΔS) between the redox couple and the concentration ratio difference (ΔC_r) between the hot and cold sides of the LTC. Typically, the concentration gradient is thermodynamically unstable and tend to spontaneously decays into a homogeneous stable state (Fig. 1, left), where ΔC_r equals zero [13, 28]. Consequently, the S_e for the traditional LTC is driven solely by ΔS. The ΔS can be increased through the addition of specific organic solvents or specific additives [9, 36]. However, their role is single and they may have minimal or even opposing impacts on the improvement of redox kinetics within the LTC [36, 37]. Yu et al. proposed a thermosensitive crystallization strategy that enhances S_e through the contributions of both ΔS and ΔC_r [28]. In the thermodynamically stable state, a concentration gradient is established within LTC, which not only enhances S_e but also effectively suppresses thermal conductivity without scarifying kinetic performance.

To further boost S_e, we establish a Cu^{2+} concentration gradient in $CuCl/CuCl_2$ solution using the ammonium sulfate ($(NH_4)_2SO_4$) to induce thermosensitive crystallization (Fig. 1, right). Specifically, the addition of $(NH_4)_2SO_4$ preferentially binds Cu^{2+} to form thermosensitive crystals on the cold side (top), where the crystals precipitate due to gravity and subsequently redissolve on the hot side (bottom). This process creates a Cu^{2+} concentration gradient, with lower concentration near the cold electrode and higher concentration near the hot electrode. We refer to this system as a thermosensitive crystallization-boosted LTC (TC-LTC). However, the relatively low concentration of the redox couple (0.15 M $CuCl/CuCl_2$) yields fewer crystals (Fig. S4). For effective thermosensitive crystallization and dissolution, sufficient crystal formation is essential. Therefore, we re-optimize the pristine LTC system, i.e., the system without thermosensitive crystallization. As the solubility of CuCl has reached its maximum under the given solvent conditions, we opted to increase only the concentration of $CuCl_2$ during the re-optimization process. By increasing the $CuCl_2$ concentration, we can enhance the number of crystals formed. When the concentration of $CuCl_2$ is increased from 0.15 to 0.4 M, the S_e of the system reaches its maximum (Fig. S4). The optimal composition for the pristine LTC is determined to be 0.15 M CuCl/0.4 M $CuCl_2$. The pristine LTC not only has a high S_e of 1.47 mV K^{-1} but also exhibits fast rapid kinetics, which are comparable to those of the 0.4 M $Fe(CN)_6^{3-}/Fe(CN)_6^{4-}$ benchmark system (Figs. S2, S5, S6). Moreover, the short-circuit current density (J_{sc}) does not fluctuate significantly over 12 h at a temperature difference (ΔT) of 40 K, indicating excellent stability for the pristine system.

The addition of $(NH_4)_2SO_4$ causes a color change in the $CuCl/CuCl_2$ solution, shifting from dark green to light blue, as blue crystals form (Figs. 2a and S7). The light blue supernatant suggests a decrease in Cu^{2+} concentration. To further confirm the specific binding of $(NH_4)_2SO_4$ to Cu^{2+}, X-ray photoelectron spectroscopy (XPS) analysis is used (Fig. 2b, c). The peaks at 954.2 eV and 934.4 eV correspond to Cu(II) $2p_{1/2}$ and Cu(II) $2p_{3/2}$, while the peaks at 952.0 eV and 932.1 eV are assigned to Cu(I) $2p_{1/2}$ and Cu(I) $2p_{3/2}$ [38]. These results confirm that Cu^{2+} predominantly resides within the crystals, whereas Cu^+ is primarily found in the supernatant. Additionally, this interaction between ammonium (NH_4^+) and Cu^{2+} in the crystals is supported by Fourier-transform infrared spectroscopy (FTIR) (Fig. S8).

The thermosensitive crystals, forming at the cold end and dissolving at the hot end, induce a copper ion concentration gradient, creating a ΔC_r. We measure the concentration ratio profile of $[Cu^{2+}]/[Cu^+]$ in the TC-LTC under varying ΔT from UV–Vis absorption spectra (Figs. 2d, S9–S11, and Note S2). At the cold side (293 K), nearly complete crystallization of Cu^{2+} led to low $[Cu^{2+}]/[Cu^+]$ ratio of ~0.27. In contrast, as the temperature increased on the hot side, rapid dissolution of the crystals resulted in a $[Cu^{2+}]/[Cu^+]$ ratio of 2.66 at 333 K. This creates a substantial ΔC_r between the electrodes, which rises with increasing ΔT. Given that S_e is synergistically influenced by both ΔS and ΔC_r, the voltage output of the TC-LTC shows significant enhancement (Figs. 2e and S12). The experimentally measured voltage values agree with those simulated using Eq. S6 and the measured $[Cu^{2+}]/[Cu^+]$ ratios. The maximum S_e achieved is 2.93 mV K^{-1}, which is nearly double that of the original LTC system (1.47 mV K^{-1}). Further optimization of the $(NH_4)_2SO_4$ addition (Figs. 2f, and S13, S14) indicates that a concentration of 4 M achieves complete crystallization of Cu^{2+} at lower temperatures, leading to the largest concentration gradient and thus maximizing S_e. Higher $(NH_4)_2SO_4$ concentrations result in decreased ΔC_r due to concomitant

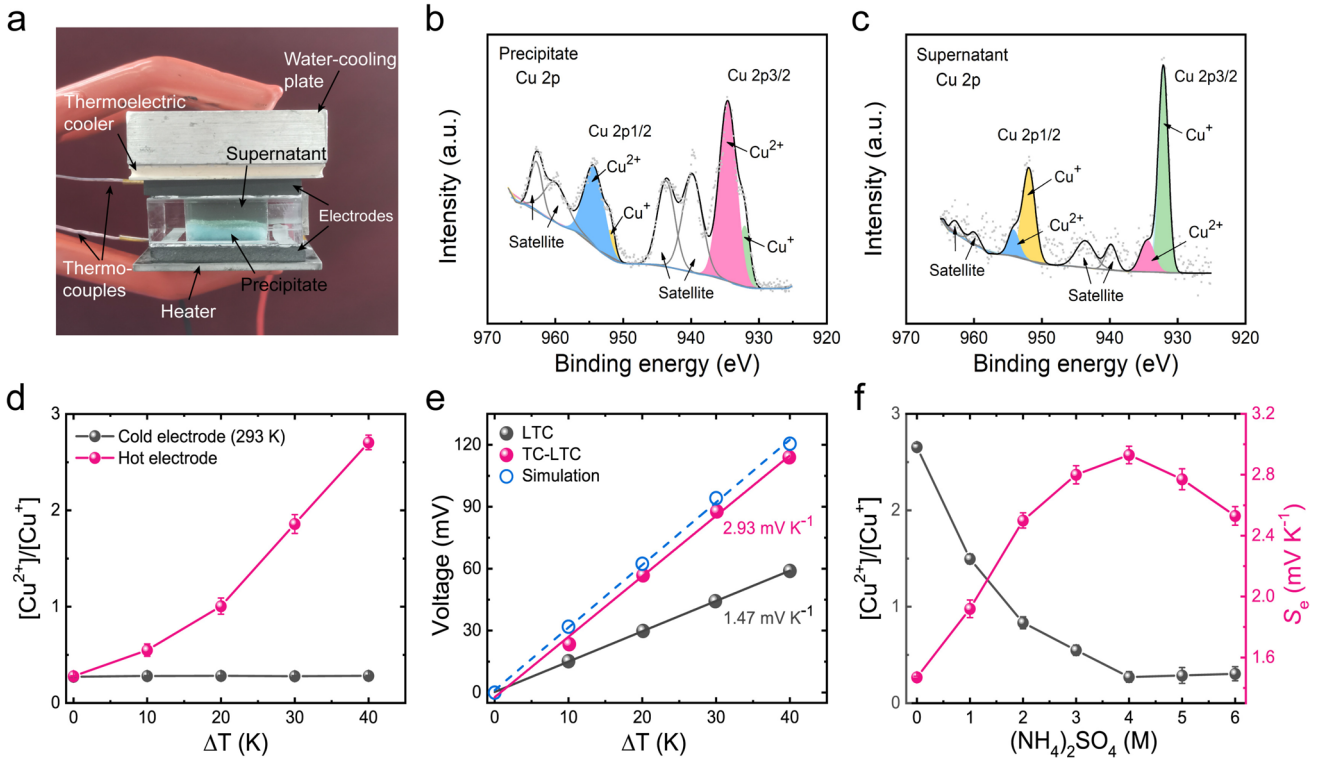

Fig. 2 Crystallization-inducing enhancement of the S_e in the TC-LTC. **a** Photograph of a single planar TC-LTC cell. The water-cooling plate and thermoelectric cooler work together to maintain the cold side temperature at 293 K. Cu 2*p* XPS spectra for dried powders from **b** the precipitate and **c** the supernatant in the $(NH_4)_2SO_4$-added electrolytes. **d** $[Cu^{2+}]/[Cu^+]$ concentration ratio at the cold and hot electrodes as a function of the temperature difference (ΔT). **e** Open-circuit voltage (V_{oc}) of the LTC and TC-LTC at different ΔT values, with simulated results (dashed line) aligning with experimental data. **f** $[Cu^{2+}]/[Cu^+]$ concentration ratio in the electrolyte at 293 K and corresponding S_e values with the addition of $(NH_4)_2SO_4$ at different concentrations

crystallization of Cu^+, which ultimately leads to a reduction in S_e.

To illustrate the underlying mechanisms of thermosensitive crystallization, we systematically investigate various monovalent cation sulfates as additives. The ability to induce crystallization is observed only with potassium (K^+), ammonium (NH_4^+) and tetramethylammonium (Tma^+) (Figs. 3a and S15). Subsequently, we examine the crystal structure using XRD (Fig. 3b). The crystals induced by $(NH_4)_2SO_4$, K_2SO_4, and $(Tma)_2SO_4$ are identified as $(NH_4)_2Cu(SO_4)_2{\bullet}6H_2O$, $K_2Cu(SO_4)_2{\bullet}6H_2O$, and $(Tma)_2Cu(SO_4)_2{\bullet}H_2O$, respectively [13, 39]. These double sulfates of divalent metals with various monovalent cations could be effectively explained based on the hard–soft acid–base (HSAB) principle, which states that hard Lewis acids preferentially bind with hard Lewis bases and soft Lewis acids with soft Lewis bases [40, 41]. In order to co-crystallize, the complex cation and the complex anion must have similar acid and base strengths [42]. As a typical intermediate hardness cation, Cu^{2+} is considered to coordinate with either H_2O molecules or anions during the formation of the double salts, depending on the relative proportions of H_2O and anions and the hardness of the second cation [13]. In the pristine electrolyte solution (0.9 M NH_4Cl and 0.1 M HCl), Cl^- progressively replaces water molecules in the hydrated $[Cu(H_2O)_6]^{2+}$ complex, forming cupric-chloro complexes such as $[CuCl(H_2O)_5]^+$ and $[CuCl_2(H_2O)_4]^0$ [43]. However, upon the introduction of sulfates, the increased sulfate concentration (4 M) promotes coordination between Cu^{2+} and SO_4^{2-}, facilitating the formation of a softer complex anion. Moreover, the harder second cations Li^+, Na^+ and guanidinium (Gdm^+) do not induce Cu^{2+} crystallization, likely due to unfavorable HSAB interactions. In contrast, the softer second cations NH_4^+, K^+, and Tma^+ could potentially form double salts with softer complex anion composed of with Cu^{2+} and SO_4^{2-}.

https://doi.org/10.1007/s40820-025-01977-w

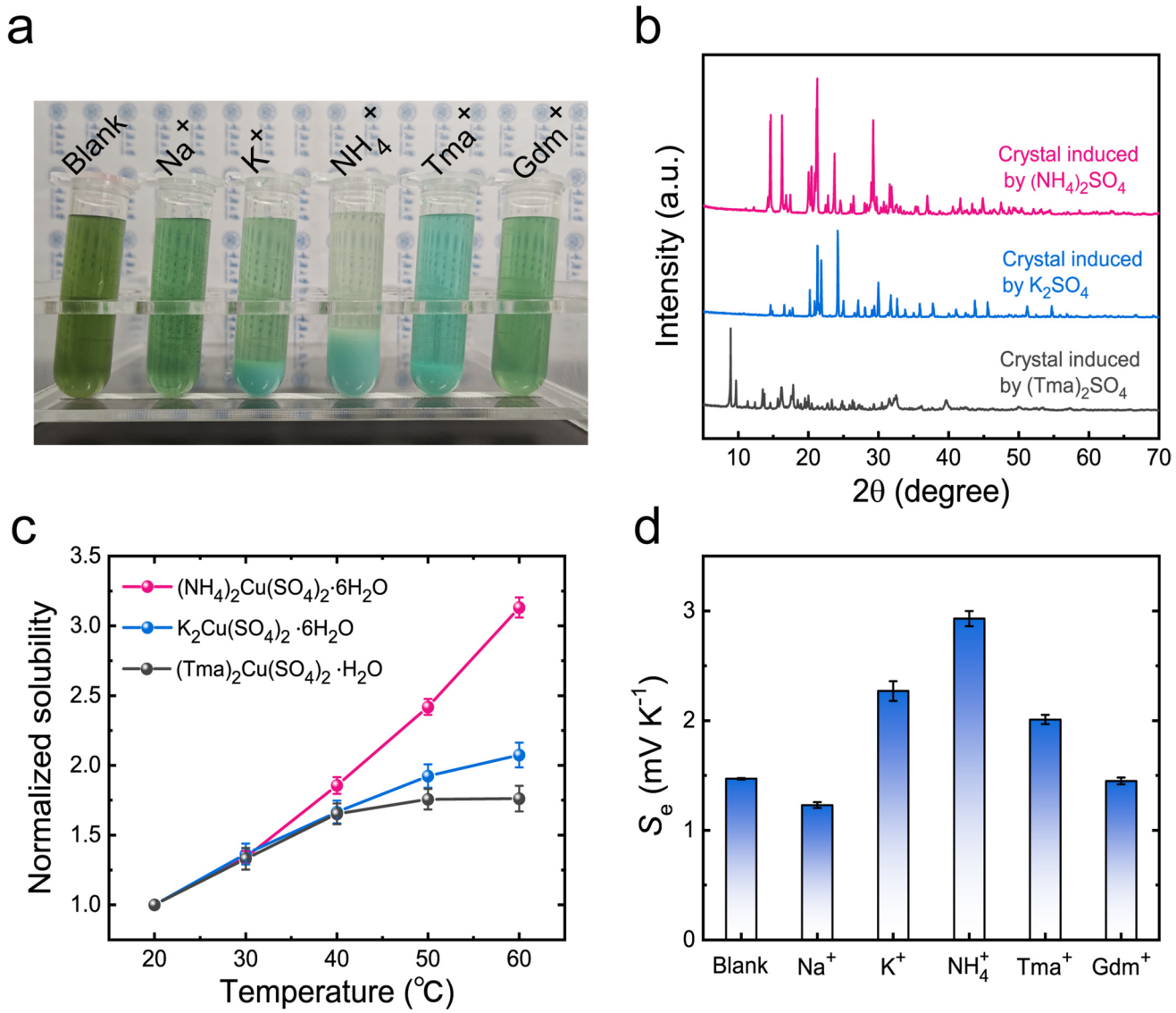

Fig. 3 Various additives for inducing thermosensitive crystallization and enhancing S_e. **a** Photographs of the electrolyte with various additives at 293 K. **b** XRD patterns of the crystals induced by various additives, confirming their identities as $(NH_4)_2Cu(SO_4)_2{\cdot}6H_2O$, $K_2Cu(SO_4)_2{\cdot}6H_2O$ and $(Tma)_2Cu(SO_4)_2{\cdot}H_2O$, respectively. **c** Normalized solubility of the three crystals as a function of temperature. **d** Comparison of S_e values for the thermocell using various additives

The thermosensitive solubility of Cu^{2+}-associated crystals is a critical for achieving a high S_e. Investigation of temperature-dependent solubility reveals that the $(NH_4)_2SO_4$-induced crystals exhibit the highest thermosensitive solubility, resulting in the greatest concentration difference with increasing temperature (Figs. 3c and S16, S17). Thermodynamic theory, captured by the equation $\Delta G = \Delta H - T\Delta S$, explains the differences in thermosensitivity among the crystals. Generally, crystals that undergo significant entropy changes (ΔS) combined with small enthalpy changes (ΔH) upon dissolution lead to a notable decrease in Gibbs free energy (ΔG) with a slightly increase in temperature, resulting in high thermosensitivity [28]. The crystal induced by $(NH_4)_2SO_4$ contains six hydrated water molecules and features the relatively large NH_4^+ cation, resulting in the highest structural complexity and a large ΔS. This highly hydrated crystal is less tightly bound and exhibits low lattice energy [44], which translates to a small ΔH during dissolution. Consequently, this unique

characteristic contributes to the highest S_e observed in the $(NH_4)_2SO_4$-enhanced TC-LTC system (Figs. 3d and S18).

The power output of the LTCs is influenced not only by the thermodynamic parameter S_e, but also by the current density [8]. Electrodes play a significant role in current delivery, particularly the microstructures of the electrodes [26, 45]. Initial experiments utilize a cost-effective graphite plate; however, its planar structure and limited specific surface area restrict the kinetic rates of the thermocell. In contrast, porous carbon electrodes offer a larger specific surface area, providing more active sites for redox reactions per unit volume, which contributes to a higher current density [46, 47]. Carbon cloth, known for its large specific surface area, is widely employed as an electrode material in the fields of energy storage and conversion [48–50]. To further enhance the specific surface area, an etched carbon cloth electrode is prepared through alkalization treatment followed by annealing at 600 °C (Fig. S19). The alkalization treatment involves soaking the carbon cloth in a 1 M KOH solution at 70 °C, which improves its hydrophilicity (Fig. S20). This enhancement facilitates easier access of the aqueous electrolyte to the carbon cloth, likely due to the formation of oxygen-containing functional groups [51, 52]. The alkalized carbon cloth electrode is designated as CC-Alkali. During the subsequent annealing process, residual KOH in the carbon cloth etches the surfaces of the carbon fibers, creating numerous tiny pores and further increasing the specific surface area [53]. The resulting electrode is referred to as CC-Alkali+A. Details of the etching mechanism are provided in Note S3. As the annealing time is extended, the density of surface micropores gradually increases (Figs. S21 and S22). However, when the annealing time reaches 7 h, the fibers exhibit ulceration, which leads to fiber breakage (Fig. S23).

Subsequently, we assembled LTC and TC-LTC devices using the electrodes described above (Fig. 4a). In brief, a plastic cell is filled with an electrolyte and sealed with treated carbon cloth, followed by graphite plates (GPs), which serve as the electrodes. Based on the assessments of current output of the LTC, we optimized the annealing time to 5 h (Fig. S24). A comparison of different types of electrodes used in the LTC is presented in Fig. 4b. The J_{sc} of the LTC utilizing the CC-Alkali+A electrodes reaches 105.23 A m^{-2}, which is greater than that of the LTC with GP electrodes or CC-Alkali electrodes. Correspondingly, maximum power density P_{max} of this LTC is significantly increased. To understand this enhancement, we leverage the electroactive surface area (ESA), defined as the fraction of the electrode surface that is electrochemically active and participates in Faradaic reactions. The ESA provides a direct measure of the number of active sites and is thus a more relevant metric for electrochemical performance than geometric area [54]. Experimentally, the ESA could be determined from the peak current density (I_p) in the cyclic voltammograms (CVs) of the electrodes (Fig. 4c). According to the Randles–Sevcik equation [55], a high faradaic peak current of an electrode exhibiting reversible kinetics indicates a high ESA [8, 56]. The ESAs of the GP, CC-Alkali, and CC-Alkali+A electrodes are estimated to be 3.77, 4.93, and 6.31 cm^2, respectively. Generally, a higher ESA corresponds to a higher P_{max} (Fig. 4d). Furthermore, the CC-Alkali+A electrode also demonstrates a lower charge transfer resistance (R_{ct}, represented by the diameter of the semicircle in a Nyquist plot) (Fig. 4e), which facilitates improved charge transport.

When utilizing the same GP electrodes, both the S_e and J of the TC-LTC system are enhanced compared to the LTC system (Fig. 4f). This increase in current density is attributed to the thermosensitive crystallization process. In TC-LTC system, a low local concentration of Cu^{2+} near the cold electrode promotes the oxidation reaction ($Cu^+ \rightarrow Cu^{2+} + e^-$), while a high local concentration of Cu^{2+} near the hot electrode enhances the reduction reaction of ($Cu^{2+} + e^- \rightarrow Cu^+$). The cell employing CC-Alkali+A electrodes in the TC-LTC, which represents an optimized electrolyte and electrode system, achieves a P_{max} of 6.35 W m^{-2} at a ΔT of 40 K. This is 7.74 times greater than that of the LTC system using GP electrodes (0.82 W m^{-2}) and 1.97 times greater than that of the TC-LTC system with GP electrodes (3.23 W m^{-2}), as shown in Fig. 4f. Additionally, the TC-LTC displays remarkable enhancements in output compared to the LTC with the same CC-Alkali+A electrodes across various ΔT values (Figs. 4g and S25). The P_{max} $(\Delta T)^{-2}$ of our optimized system reaches 3.97 mW m^{-2} K^{-2}, remarkably surpassing those of current n-type LTCs, including $[Co(bpy)_3]^{2+}/[Co(bpy)_3]^{3+}$ system [37, 57, 58], Cu/Cu^{2+} system [13, 59, 60], I^-/I_3^- system [15, 21, 61], and various Fe^{2+}/Fe^{3+} systems [33–35, 46, 47] (Fig. 4h and Table S1). In comparison to p-type $Fe(CN)_6^{3-}/Fe(CN)_6^{4-}$ systems, our optimized system outperforms most $Fe(CN)_6^{3-}/Fe(CN)_6^{4-}$-based LTCs [9, 26, 33, 36], except for the one reported by Yu et al. [28]. This motivates us to explore more suitable additives for thermosensitive crystallization to achieve higher S_e values and to

 https://doi.org/10.1007/s40820-025-01977-w

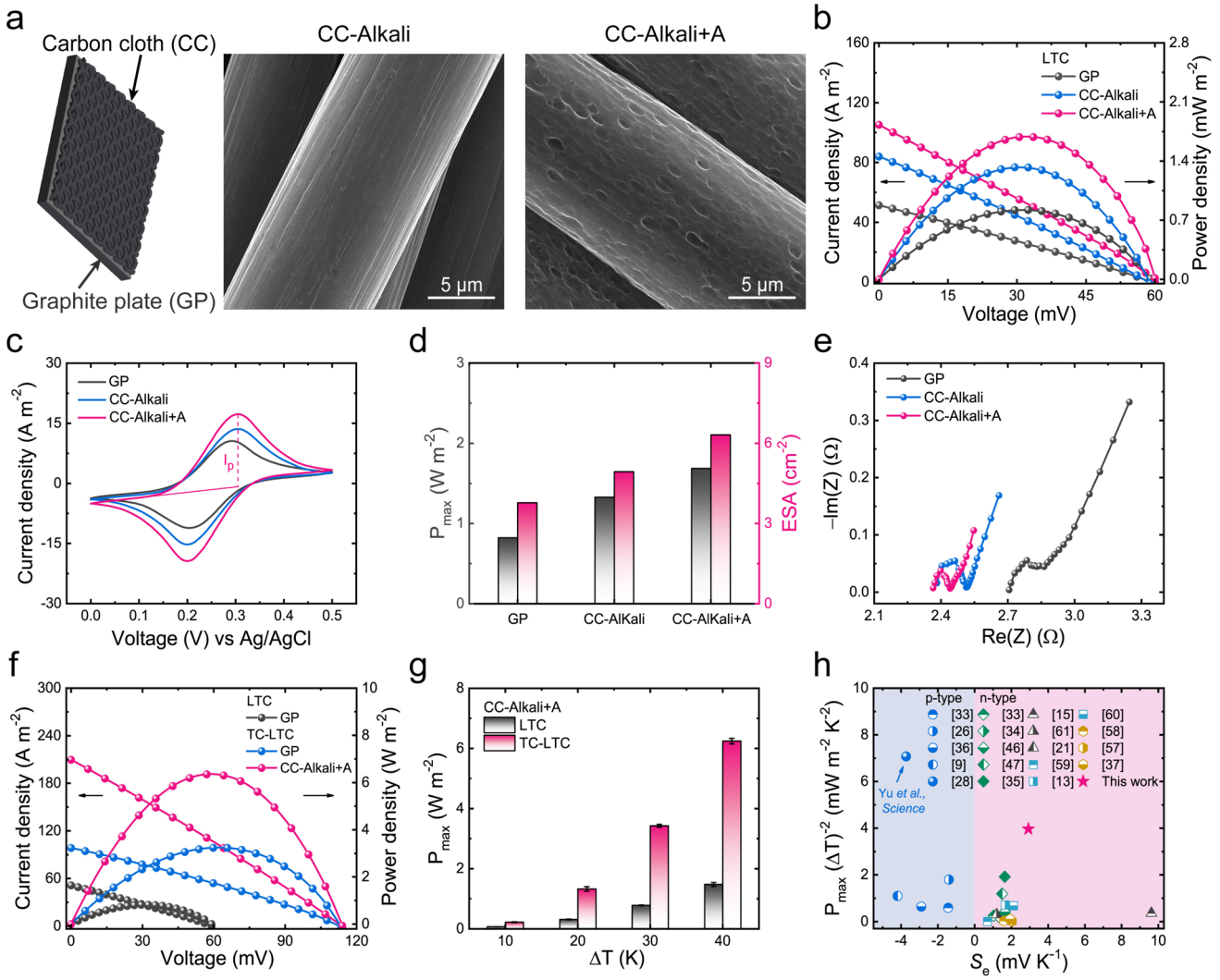

Fig. 4 Electrode optimization of the Cu-based thermocells. **a** Diagram of electrode structure along with SEM images of the surface of carbon cloth. The alkalized carbon cloth electrode is labeled as CC-Alkali, while the etched carbon cloth electrode, produced through alkalization and annealing treatment, is labeled as CC-Alkali+A. **b** Current–voltage and power–voltage curves for the LTC using different electrodes at a ΔT of 40 K. **c** Cyclic voltammograms of different electrodes. **d** Maximum output power density P_{max} of LTC with different electrodes and electroactive surface area (ESA) values. **e** Electrochemical impedance spectra of different electrodes. **f** Current–voltage and power–voltage curves for the LTC and TC-LTC using different electrodes at a ΔT of 40 K. **g** Maximum power density (P_{max}) for the LTC and TC-LTC utilizing CC-Alkali+A electrodes at varying ΔT. **h** Comparison of P_{max} $(\Delta T)^{-2}$ and S_e values for this work and the other LTCs

develop more effective electrode optimization strategies for faster reaction kinetics. Moreover, we have evaluated the cost-performance metric (CPM) of various thermoelectric systems by considering the prices of raw materials. Compared to inorganic solid-state thermoelectric cells (ITECs) and organic solid-state thermoelectric cells (OTECs), our TC-LTC system demonstrates a potentially more cost-effective profile, as detailed in Table S2.

Finally, we design a TC-LTC module by connecting 20 cells to demonstrate the viability for scale-up (Fig. 5a). Each isolated cell maintains the same electrode configuration and size as the planar cells tested earlier, and the isolated cells are connected in series by Cu wires. The module generates an open-circuit voltage (V_{oc}) of 2.14 V and a short-circuit current of 41.95 mA, resulting in a P_{max} of 27.19 mW under a ΔT of 40 K (Fig. 5b, c). Relative to a single TC-LTC, the loss of current is attributed to increased internal resistance from the series connections [33]. Given the considerable power output, the module is capable of directly driving various electronic devices, including a thermohygrometer,

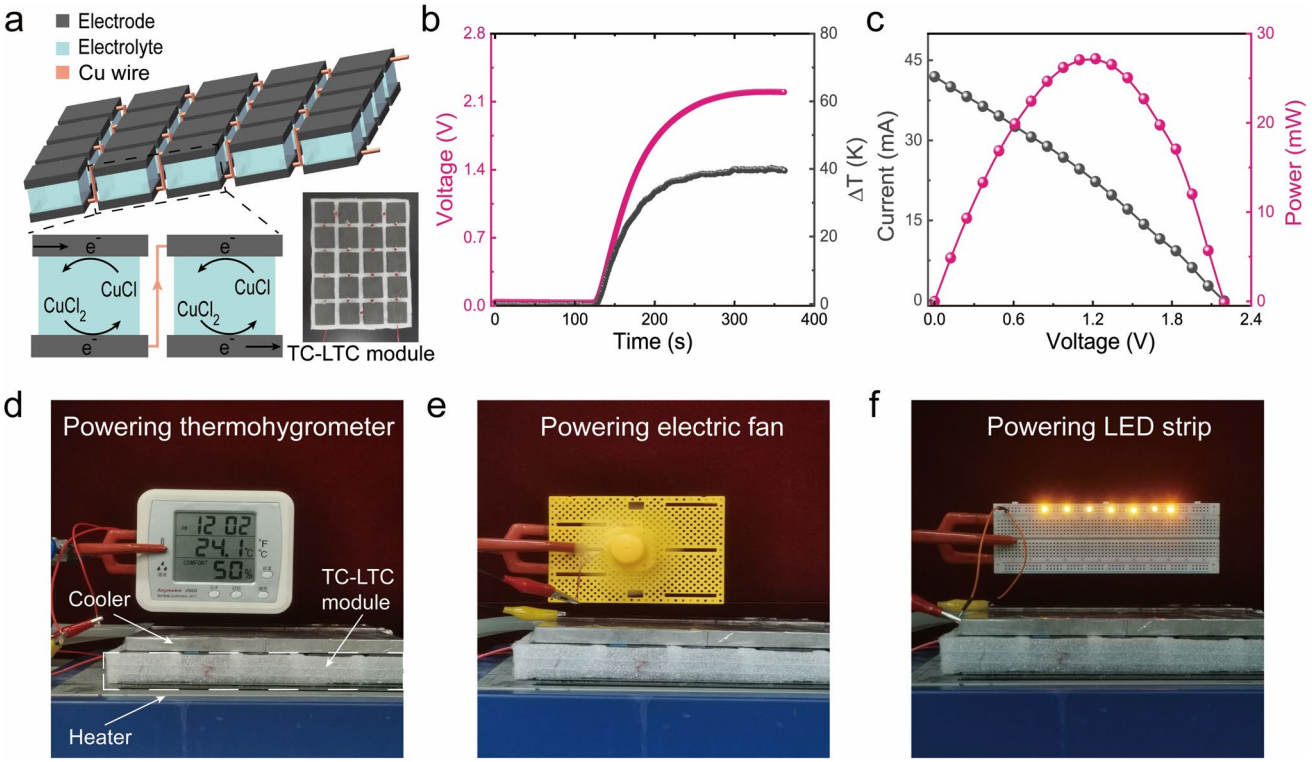

Fig. 5 Electricity generation and demonstration of using a TC-LTC module to power electronic devices. **a** Schematic representation and photograph of a TC-LTC module containing 20 units connected in series. **b** Real-time voltage curves of the module with increasing temperature difference (ΔT). **c** Current–voltage curve and corresponding power output of the module at $\Delta T = 40$ K. Image of the module directly powering various small electronic devices, including **d** a thermohygrometer, **e** an electric fan, and **f** an LED strip

an electric fan, and a light-emitting diode (LED) strip (Fig. 5d–f, and Movie S1). This suggests that the Cu-based TC-LTC we developed shows excellent potential for recovering low-grade heat.

4 Conclusions

In summary, we have achieved a high-performance LTC through the synergistic thermodynamic and kinetic engineering of a novel Cu^{+}/Cu^{2+} system, resulting in a high S_e of 2.93 mV K^{-1} and a power density of 6.35 W m^{-2} at ΔT of 40 K. Specifically, we developed a thermosensitive crystal, $(NH_4)_2Cu(SO_4)_2{\cdot}6H_2O$, induced by ammonium sulfate, which enables both a significant entropy change to enhance S_e and a concentration gradient simultaneously to improve the redox reaction of Cu^{+}/Cu^{2+}. Furthermore, we design an etched carbon cloth electrode with high hydrophilicity and a large electroactive area to further boost the redox kinetics. Consequently, our optimized Cu^{+}/Cu^{2+}-based LTC achieves a remarkable $P_{max}(\Delta T)^{-2}$ of 3.97 mW m^{-2} K^{-2}, representing the best performance among current n-type LTCs. A prototype module consisting of 20 units successfully generates usable electrical energy, capable of directly powering small electronics, demonstrating the potential of this system for efficient low-grade heat harvesting. Prospectively, we will further enhance the kinetic properties of the Cu^{+}/Cu^{2+} system by optimizing electrode materials and structures, as well as increasing the concentration of $CuCl/CuCl_2$, to enable highly efficient p–n integrated devices with thermosensitive crystallization processes.

Acknowledgements This work was financially supported by research grants from Innovative Research Group Project of National Natural Science Foundation of China (52021004), the National Key Research and Development Program of China (2022YFB3803300), the National Natural Science Foundation of China (62474026, 62205140, 12204071), and the China Postdoctoral Science Foundation (2022M710532).

Author Contributions KS and WF conceived the idea. WF, ZO, YW, ZL, and QH contributed to material preparation and

https://doi.org/10.1007/s40820-025-01977-w

characterization. KS, WF, YW, ZL, PZ, and XL analyzed the data. WF prepared the manuscript. KS, YZ, LH, CL, and JO revised the manuscript. KS was involved in funding acquisition and supervision. All authors discussed the results and approved the final version of the manuscript.

Declarations

Conflict of interest The authors declare no interest conflict. They have no known competing financial interests or personal relationships that could have appeared to influence the work reported in this paper.

Supplementary Information The online version contains supplementary material available at https://doi.org/10.1007/s40820-025-01977-w.

References

1. X. Kou, R. Wang, S. Du, Z. Xu, X. Zhu, Heat pump assists in energy transition: challenges and approaches. DeCarbon **3**, 100033 (2024). https://doi.org/10.1016/j.decarb.2023.100033
2. L. Hu, H. Zheng, S. Yang, X. Liu, Y.-M. Du et al., Thermal-to-electrical conversion based on salinity gradient driven by evaporation. Small **20**(28), e2311129 (2024). https://doi.org/10.1002/smll.202311129
3. M. Luberti, R. Gowans, P. Finn, G. Santori, An estimate of the ultralow waste heat available in the European Union. Energy **238**, 121967 (2022). https://doi.org/10.1016/j.energy.2021.121967
4. C. Forman, I.K. Muritala, R. Pardemann, B. Meyer, Estimating the global waste heat potential. Renew. Sustain. Energy Rev. **57**, 1568–1579 (2016). https://doi.org/10.1016/j.rser.2015.12.192
5. A. Tarancón, Powering the IoT revolution with heat. Nat. Electron. **2**(7), 270–271 (2019). https://doi.org/10.1038/s41928-019-0276-4
6. M. Massetti, F. Jiao, A.J. Ferguson, D. Zhao, K. Wijeratne et al., Unconventional thermoelectric materials for energy harvesting and sensing applications. Chem. Rev. **121**(20), 12465–12547 (2021). https://doi.org/10.1021/acs.chemrev.1c00218
7. Q. Le, H. Cheng, J. Ouyang, Flexible combinatorial ionic/electronic thermoelectric converters to efficiently harvest heat from both temperature gradient and temperature fluctuation. DeCarbon **1**, 100003 (2023). https://doi.org/10.1016/j.decarb.2023.100003
8. H. Im, T. Kim, H. Song, J. Choi, J.S. Park et al., High-efficiency electrochemical thermal energy harvester using carbon nanotube aerogel sheet electrodes. Nat. Commun. **7**, 10600 (2016). https://doi.org/10.1038/ncomms10600
9. J. Duan, G. Feng, B. Yu, J. Li, M. Chen et al., Aqueous thermogalvanic cells with a high Seebeck coefficient for low-grade heat harvest. Nat. Commun. **9**(1), 5146 (2018). https://doi.org/10.1038/s41467-018-07625-9
10. G. Li, D. Dong, G. Hong, L. Yan, X. Zhang et al., High-efficiency cryo-thermocells assembled with anisotropic holey graphene aerogel electrodes and a eutectic redox electrolyte. Adv. Mater. **31**(25), 1901403 (2019). https://doi.org/10.1002/adma.201901403
11. Y. Liu, Q. Zhang, G.O. Odunmbaku, Y. He, Y. Zheng et al., Solvent effect on the seebeck coefficient of Fe^{2+}/Fe^{3+} hydrogel thermogalvanic cells. J. Mater. Chem. A **10**(37), 19690–19698 (2022). https://doi.org/10.1039/d1ta10508f
12. Y. Chen, Q. Huang, T.-H. Liu, X. Qian, R. Yang, Effect of solvation shell structure on thermopower of liquid redox pairs. EcoMat **5**(9), e12385 (2023). https://doi.org/10.1002/eom2.12385
13. B. Yu, H. Xiao, Y. Zeng, S. Liu, D. Wu et al., Cost-effective n-type thermocells enabled by thermosensitive crystallizations and 3D multi-structured electrodes. Nano Energy **93**, 106795 (2022). https://doi.org/10.1016/j.nanoen.2021.106795
14. I. Burmistrov, N. Kovyneva, N. Gorshkov, A. Gorokhovsky, A. Durakov et al., Development of new electrode materials for thermo-electrochemical cells for waste heat harvesting. Renew. Energy Focus **29**, 42–48 (2019). https://doi.org/10.1016/j.ref.2019.02.003
15. Y. Han, J. Zhang, R. Hu, D. Xu, High-thermopower polarized electrolytes enabled by methylcellulose for low-grade heat harvesting. Sci. Adv. **8**(7), eabl5318 (2022). https://doi.org/10.1126/sciadv.abl5318
16. J. Duan, B. Yu, K. Liu, J. Li, P. Yang et al., P–N conversion in thermogalvanic cells induced by thermo-sensitive nanogels for body heat harvesting. Nano Energy **57**, 473–479 (2019). https://doi.org/10.1016/j.nanoen.2018.12.073
17. W. Fang, H. Luo, I. Mwamburi Mwakitawa, F. Yuan, X. Lin et al., Boosting thermogalvanic cell performance through synergistic redox and thermogalvanic corrosion. Chemsuschem **18**(5), e202401749 (2025). https://doi.org/10.1002/cssc.202401749
18. B. Guo, Y. Hoshino, F. Gao, K. Hayashi, Y. Miura et al., Thermocells driven by phase transition of hydrogel nanoparticles. J. Am. Chem. Soc. **142**(41), 17318–17322 (2020). https://doi.org/10.1021/jacs.0c08600

19. Y. Liu, M. Cui, W. Ling, L. Cheng, H. Lei et al., Thermo-electrochemical cells for heat to electricity conversion: from mechanisms, materials, strategies to applications. Energy Environ. Sci. **15**(9), 3670–3687 (2022). https://doi.org/10.1039/d2ee01457b
20. J. Duan, B. Yu, L. Huang, B. Hu, M. Xu et al., Liquid-state thermocells: opportunities and challenges for low-grade heat harvesting. Joule **5**(4), 768–779 (2021). https://doi.org/10.1016/j.joule.2021.02.009
21. H. Zhou, T. Yamada, N. Kimizuka, Supramolecular thermo-electrochemical cells: enhanced thermoelectric performance by host–guest complexation and salt-induced crystallization. J. Am. Chem. Soc. **138**(33), 10502–10507 (2016). https://doi.org/10.1021/jacs.6b04923
22. P. Peng, J. Zhou, L. Liang, X. Huang, H. Lv et al., Regulating thermogalvanic effect and mechanical robustness via redox ions for flexible quasi-solid-state thermocells. Nano-Micro Lett. **14**(1), 81 (2022). https://doi.org/10.1007/s40820-022-00824-6
23. X. Lu, D. Xie, K. Zhu, S. Wei, Z. Mo et al., Swift assembly of adaptive thermocell arrays for device-level healable and energy-autonomous motion sensors. Nano-Micro Lett. **15**(1), 196 (2023). https://doi.org/10.1007/s40820-023-01170-x
24. B. Xie, Z. Chen, H. Li, Z. Liu, M. Li et al., Stratified triphasic thermocells with boosted thermopower enabled by entropy-concentration dual regulation strategy. Adv. Funct. Mater. (2025). https://doi.org/10.1002/adfm.202519934
25. Z. Liu, D. Wu, S. Wei, K. Xing, M. Li et al., MXene hollow microsphere-boosted nanocomposite electrodes for thermocells with enhanced thermal energy harvesting capability. ACS Nano **19**(3), 3392–3402 (2025). https://doi.org/10.1021/acsnano.4c12294
26. L. Zhang, T. Kim, N. Li, T.J. Kang, J. Chen et al., High power density electrochemical thermocells for inexpensively harvesting low-grade thermal energy. Adv. Mater. **29**(12), 1605652 (2017). https://doi.org/10.1002/adma.201605652
27. S. Wei, J. Ma, D. Wu, B. Chen, C. Du et al., Constructing flexible film electrode with porous layered structure by MXene/SWCNTs/PANI ternary composite for efficient low-grade thermal energy harvest. Adv. Funct. Mater. **33**(13), 2209806 (2023). https://doi.org/10.1002/adfm.202209806
28. B. Yu, J. Duan, H. Cong, W. Xie, R. Liu et al., Thermosensitive crystallization-boosted liquid thermocells for low-grade heat harvesting. Science **370**(6514), 342–346 (2020). https://doi.org/10.1126/science.abd6749
29. J.H. Kim, Y. Han, G. Shin, J.G. Jeon, H.J. Kim et al., Separation-free planar interconnection for thermo-electrochemical cells. ACS Appl. Energy Mater. **5**(10), 13053–13061 (2022). https://doi.org/10.1021/acsaem.2c02778
30. X. Yu, Z. Shen, G. Qian, G. Lu, H. Liu et al., Synergistic improvement of Seebeck coefficient and power density of an aqueous thermocell using natural convection for low-grade heat utilization. Appl. Therm. Eng. **231**, 121004 (2023). https://doi.org/10.1016/j.applthermaleng.2023.121004
31. R. Hu, B.A. Cola, N. Haram, J.N. Barisci, S. Lee et al., Harvesting waste thermal energy using a carbon-nanotube-based thermo-electrochemical cell. Nano Lett. **10**(3), 838–846 (2010). https://doi.org/10.1021/nl903267n
32. M.S. Romano, N. Li, D. Antiohos, J.M. Razal, A. Nattestad et al., Carbon nanotube—reduced graphene oxide composites for thermal energy harvesting applications. Adv. Mater. **25**(45), 6602–6606 (2013). https://doi.org/10.1002/adma.201303295
33. K. Kim, S. Hwang, H. Lee, Unravelling ionic speciation and hydration structure of Fe(III/II) redox couples for thermo-electrochemical cells. Electrochim. Acta **335**, 135651 (2020). https://doi.org/10.1016/j.electacta.2020.135651
34. M.A. Buckingham, F. Marken, L. Aldous, The thermoelectrochemistry of the aqueous iron(II)/iron(III) redox couple: significance of the anion and pH in thermogalvanic thermal-to-electrical energy conversion. Sustain. Energy Fuels **2**(12), 2717–2726 (2018). https://doi.org/10.1039/c8se00416a
35. S.-M. Jung, S.-Y. Kang, B.-J. Lee, J. Lee, J. Kwon et al., Fe─N─C electrocatalyst for enhancing Fe(II)/Fe(III) redox kinetics in thermo-electrochemical cells. Adv. Funct. Mater. **33**(45), 2304067 (2023). https://doi.org/10.1002/adfm.202304067
36. T. Kim, J.S. Lee, G. Lee, H. Yoon, J. Yoon et al., High thermopower of ferri/ferrocyanide redox couple in organic-water solutions. Nano Energy **31**, 160–167 (2017). https://doi.org/10.1016/j.nanoen.2016.11.014
37. K. Laws, M.A. Buckingham, M. Farleigh, M. Ma, L. Aldous, High seebeck coefficient thermogalvanic cells via the solvent-sensitive charge additivity of cobalt 1, 8-diaminosarcophagine. Chem. Commun. **59**(16), 2323–2326 (2023). https://doi.org/10.1039/d2cc05413b
38. M. He, Z. Wang, D. Xiang, D. Sun, Y.K. Chan et al., A H_2S-evolving alternately-catalytic enzyme bio-heterojunction with antibacterial and macrophage-reprogramming activity for all-stage infectious wound regeneration. Adv. Mater. **36**(35), e2405659 (2024). https://doi.org/10.1002/adma.202405659
39. R.S. Vilela, T.L. Oliveira, F.T. Martins, J.A. Ellena, F. Lloret et al., Synthesis, crystal structure and magnetic properties of the helical oxalate-bridged copper(II) chain$\{[(CH_3)_4N]_2[Cu(C_2O_4)_2]\cdot H_2O\}$n. Comptes Rendus Chim. **15**(10), 856–865 (2012). https://doi.org/10.1016/j.crci.2012.04.006
40. R.G. Pearson, Hard and soft acids and bases. J. Am. Chem. Soc. **85**(22), 3533–3539 (1963). https://doi.org/10.1021/ja00905a001
41. T.-L. Ho, Hard soft acids bases (HSAB) principle and organic chemistry. Chem. Rev. **75**(1), 1–20 (1975). https://doi.org/10.1021/cr60293a001
42. R. Duhlev, I.D. Brown, C. Balarew, Divalent metal halide double salts in equilibrium with their aqueous solutions I. Factors determining their composition. J. Solid State Chem. **95**(1), 39–50 (1991). https://doi.org/10.1016/0022-4596(91)90374-Q
43. M. Uchikoshi, Determination of the distribution of cupric chloro-complexes in hydrochloric acid solutions at 298K. J. Solut. Chem. **46**(3), 704–719 (2017). https://doi.org/10.1007/s10953-017-0597-8
44. J. Sohr, H. Schmidt, W. Voigt, Higher hydrates of lithium chloride, lithium bromide and lithium iodide. Acta Crystallogr. C

 https://doi.org/10.1007/s40820-025-01977-w

Struct. Chem. **74**(Pt 2), 194–202 (2018). https://doi.org/10.1107/S2053229618001183

45. K. Hyeon, K. June, Diffusion and current generation in porous electrodes for thermo-electrochemical cells. ACS Appl. Mater. Interfaces **11**(32), 28894–28899 (2019). https://doi.org/10.1021/acsami.9b08381
46. L. Hwan, Y. Jung, K. Hyeon, Y. Jae, K. June, Stacked double-walled carbon nanotube sheet electrodes for electrochemically harvesting thermal energy. Carbon **147**, 559–565 (2019). https://doi.org/10.1016/j.carbon.2019.03.033
47. W. Li, C. Gao, J. Ma, J. Qiu, S. Wang, Simultaneous enhancement of thermopower and ionic conductivity for N-type Fe(III/II) thermocell. Mater. Today Energy **30**, 101147 (2022). https://doi.org/10.1016/j.mtener.2022.101147
48. L.Y. Yang, H.Z. Li, L.Z. Cheng, S.T. Li, J. Liu et al., A three-dimensional surface modified carbon cloth designed as flexible current collector for high-performance lithium and sodium batteries. J. Alloys Compd. **726**, 837–845 (2017). https://doi.org/10.1016/j.jallcom.2017.08.054
49. S. Pang, L. Lin, Y. Shen, S. Chen, W. Chen et al., Surface activated commercial carbon cloth as superior electrodes for symmetric supercapacitors. Mater. Lett. **315**, 131985 (2022). https://doi.org/10.1016/j.matlet.2022.131985
50. X. Li, D. Lou, H. Wang, X. Sun, J. Li et al., Flexible supercapacitor based on organohydrogel electrolyte with long-term antifreezing and anti-drying property. Adv. Funct. Mater. **30**(52), 2007291 (2020). https://doi.org/10.1002/adfm.202007291
51. C. Qiu, L. Jiang, Y. Gao, L. Sheng, Effects of oxygen-containing functional groups on carbon materials in supercapacitors: a review. Mater. Des. **230**, 111952 (2023). https://doi.org/10.1016/j.matdes.2023.111952
52. J. Sun, C. Hu, Z. Liu, H. Liu, J. Qu, Surface charge and hydrophilicity improvement of graphene membranes *via* modification of pore surface oxygen-containing groups to enhance permeability and selectivity. Carbon **145**, 140–148 (2019). https://doi.org/10.1016/j.carbon.2018.12.098
53. Z. Zhang, J. Xi, H. Zhou, X. Qiu, KOH etched graphite felt with improved wettability and activity for vanadium flow batteries. Electrochim. Acta **218**, 15–23 (2016). https://doi.org/10.1016/j.electacta.2016.09.099
54. P. Zhu, Y. Zhao, Effects of electrochemical reaction and surface morphology on electroactive surface area of porous copper manufactured by lost carbonate sintering. RSC Adv. **7**(42), 26392–26400 (2017). https://doi.org/10.1039/c7ra04204c
55. P. Papakonstantinou, R. Kern, L. Robinson, H. Murphy, J. Irvine et al., Fundamental electrochemical properties of carbon nanotube electrodes. Fullerenes Nanotubes Carbon Nanostruct. **13**(2), 91–108 (2005). https://doi.org/10.1081/FST-200050684
56. S. Wang, Y. Li, M. Yu, Q. Li, H. Li et al., High-performance cryo-temperature ionic thermoelectric liquid cell developed through a eutectic solvent strategy. Nat. Commun. **15**(1), 1172 (2024). https://doi.org/10.1038/s41467-024-45432-7
57. T.J. Abraham, D.R. MacFarlane, J.M. Pringle, High Seebeck coefficient redox ionic liquid electrolytes for thermal energy harvesting. Energy Environ. Sci. **6**(9), 2639–2645 (2013). https://doi.org/10.1039/c3ee41608a
58. P.F. Salazar, S.T. Stephens, A.H. Kazim, J.M. Pringle, B.A. Cola, Enhanced thermo-electrochemical power using carbon nanotube additives in ionic liquid redox electrolytes. J. Mater. Chem. A **2**(48), 20676–20682 (2014). https://doi.org/10.1039/c4ta04749d
59. A.M. Bates, B. Zickel, S. Krebs, S. Mukherjee, N.D. Schuppert et al., Analytical study and experimental validation of copper II sulfate and potassium ferri/ferrocyanide thermocells using Onsager flux equations. J. Energy Resour. Technol. **139**(4), 042003 (2017). https://doi.org/10.1115/1.4036045
60. M. Wu, S. Hao, L. Qi, Y. Shi, W. Yang et al., An N-type thermogalvanic cell with a high temperature coefficient based on the $Cu/Cu(en)_2^{2+}$ redox couple. ACS Appl. Mater. Interfaces **17**(18), 26775–26783 (2025). https://doi.org/10.1021/acsami.5c03375
61. H. Wang, X. Zhuang, W. Xie, H. Jin, R. Liu et al., Thermosensitive-CsI_3-crystal-driven high-power I^-/I_3^- thermocells. Cell Rep. Phys. Sci. **3**(3), 100737 (2022). https://doi.org/10.1016/j.xcrp.2022.100737